

# Compressive-Sensing Data Reconstruction for Structural Health

## Monitoring: A Machine-Learning Approach

Yuequan Bao<sup>\*</sup>, Zhiyi Tang, Hui Li

<sup>1</sup>Key Lab of Structures Dynamic Behavior and Control of the Ministry of Education, Harbin Institute of Technology, Harbin, 150090, China

<sup>2</sup>Artificial Intelligence Lab, Harbin Institute of Technology, Harbin, 150090, China

<sup>3</sup>School of Civil Engineering, Harbin Institute of Technology, Harbin, 150090, China

### Abstract

Compressive sensing (CS) has been studied and applied in structural health monitoring for data acquisition and reconstruction, wireless data transmission, structural modal identification, and spare damage identification. The key issue in CS is finding the optimal solution for sparse optimization. In the past several years, many algorithms have been proposed in the field of applied mathematics. In this paper, we propose a machine-learning-based approach to solve the CS data-reconstruction problem. By treating a computation process as a data flow, the solving process of CS-based data reconstruction is formalized into a standard supervised-learning task. The prior knowledge, i.e., the basis matrix and the CS-sampled signals, are used as the input and the target of the network; the basis coefficient matrix is embedded as the parameters of a certain layer; and the objective function of conventional compressive sensing is set as the loss function of the network. Regularized by  $l_1$ -norm, these basis coefficients are optimized to reduce the error between the original CS-sampled signals and the masked reconstructed signals with a common optimization algorithm. In addition, the proposed network is able to handle complex bases, such as a Fourier basis. Benefiting from the nature of a multi-neuron layer, multiple signal channels can be reconstructed simultaneously. Meanwhile, the disassembled use of a large-scale basis makes the method memory-efficient. A numerical example of multiple sinusoidal waves and an example of field-test wireless data from a suspension bridge are carried out to illustrate the data-reconstruction ability of

---

<sup>\*</sup> Correspondence to: Dr. Yuequan Bao (Professor), School of Civil Engineering, Harbin Institute of Technology, Harbin, China. Artificial Intelligence Lab, Harbin Institute of Technology, Harbin, China.  
E-mail: baoyuequan@hit.edu.cn.

the proposed approach. The results show that high reconstruction accuracy can be obtained by the machine learning-based approach. In addition, the parameters of the network have clear meanings; the inference of the mapping between input and output is fully transparent, making the CS data reconstruction neural network interpretable.

## **Keywords:**

Structural health monitoring; compressive sensing; model-driven machine learning; interpretable machine learning; sparse data reconstruction

## **1 Introduction**

Structural health monitoring (SHM) is a technology used to maintain the safety of structures that has been widely used in aerospace, civil, and mechanical engineering.<sup>1-8</sup> Generally, a SHM system consists of various sensors, a data-acquisition and -transmission system, data analysis and modeling, structural health diagnosis (including data processing, data mining, damage detection, model updating, safety evaluation, and reliability analysis), alarming devices, a visualization user interface, and software as well as an operating system.<sup>7</sup>

Data acquisition is the fundamental part in a SHM system. Traditional data acquisition must obey the Nyquist-Shannon sampling theorem, which requires a signal to be sampled at least two times at the highest frequency in the signal. Thus, the amount of data collected by the SHM system will be huge. Compressive sensing (CS), also known as compressive sampling as proposed by Donoho and Candes, provides a new sampling theory for signals with sparse features in a certain domain.<sup>9, 10</sup> The signal is randomly collected, the size of which is much smaller than that recorded following the Nyquist-Shannon sampling theorem. Then, the original signal then can be exactly reconstructed with sparse optimization algorithms.<sup>9, 10</sup>

In CS theory, the raw signal  $\mathbf{y} \in \mathbb{R}^n$  can be sampled using a linear measurement,

$$\mathbf{y}_s = \Phi \mathbf{y} + \mathbf{e}, \quad (1)$$

where  $\Phi$  denotes a measurement matrix or sampling operator in an  $m \times n$  matrix,  $\mathbf{y}_s$  is the sampled signal vector, and  $e$  is the measurement noise.

As  $\Phi$  is an  $m \times n$  matrix with  $m \ll n$ , the problem of reconstructing the signal  $\mathbf{x}$  is ill-posed. However, CS theory proved that if the signal  $\mathbf{x}$  is sparse (i.e., the signal has a sparse representation in some basis  $\Psi$  or a redundant dictionary  $D$ ,  $\mathbf{y} = \Psi\mathbf{x}$  or  $\mathbf{y} = D\mathbf{x}$ ) and the  $\Phi$  satisfies the restrictive isometry property (RIP), then the coefficient  $\alpha$  can be reconstructed by the  $l_1$  optimization problem:

$$\begin{aligned} \mathbf{y} &= \Phi\Psi\mathbf{x} + e = \Theta\mathbf{x} + e . \\ \hat{\mathbf{x}} &= \min \|\mathbf{x}\|_1 \text{ such that } \|\mathbf{y} - \Theta\hat{\mathbf{x}}\|_2 \leq \varepsilon , \end{aligned} \quad (2)$$

where  $\varepsilon$  is the bound on the level of the measurement error,  $\|e\|_2 \leq \varepsilon$ .

Many algorithms have been proposed to solve the optimization problem of Eq. (2), such as basic pursuit (BP),<sup>11</sup> gradient projection for sparse reconstruction (GPSR),<sup>12</sup>  $l_1$  regularized least squares ( $l_1$ - $l_s$ )<sup>13</sup>, fixed-point continuation<sup>14</sup> (FPC) and the FPC active set<sup>15</sup> (FPC-AS), split Bregman,<sup>16</sup> the fast iterative shrinkage-thresholding algorithm,<sup>17</sup> sparse reconstruction by separable approximation (SpaRSA),<sup>18</sup> NESTA (Nesterov's algorithm),<sup>19</sup> the Bayesian methods,<sup>20</sup> and the group least absolute shrinkage and selection operator (LASSO).<sup>21</sup>

CS has been widely used in many fields, including consumer camera imaging,<sup>22,23</sup> medical magnetic-resonance imaging,<sup>13</sup> remote sensing,<sup>24</sup> seismic exploration,<sup>25</sup> and communications, especially for wireless sensor networks (WSN).<sup>26,27</sup> In SHM, the applications of CS theory have also been investigated in structural vibration data acquisition,<sup>28</sup> wireless data transmission and lost data recovery,<sup>29-34</sup> structural modal identification,<sup>35,36</sup> structural sparse damage identification,<sup>37-42</sup> and sparse heavy-vehicle-loads identification of long-span bridges.<sup>43</sup>

As mentioned above, the nature of CS is to solve an ill-posed inverse problem. By constructing an efficient objective function and regularization, the original data can be reconstructed by iterative optimization procedures. The recent advanced deep-learning techniques, as iterative methods, are naturally exploited to solve ill-posed inverse problems, especially in imaging, including image reconstruction,<sup>44-46</sup> super-resolution,<sup>47-49</sup> image denoising and inpainting,<sup>48,49</sup> and image colorization.<sup>50</sup>

<sup>51</sup> The state-of-the-art performance of the above-listed deep neural networks (DNNs) are mainly

accomplished by a large-scale data-driven strategy; meanwhile, the inner workings of the DNNs continue to be difficult to understand and interpret. More recently, several works have been devoted to incorporate machine-learning techniques and domain prior knowledge,<sup>44, 46, 52</sup> which not only accomplished superior performance for inverse-problem solving, but also have interpretable inner mechanisms. To date, little effort has been made to develop the hybrid strategy outside the field of image processing and computer vision. In this paper, by treating a computation process as a data flow,<sup>53</sup> we formalize the CS problem into a standard supervised-learning task for time-series signal reconstruction. We design a fully transparent neural network embedded with  $l_1$  regularization. Unlike conventional black-box neural networks, the parameters of the network are interpretable with clear meaning; the inference of the mapping between input and output is fully transparent; and the large-scale basis matrix is distributedly utilized, which makes the method memory-efficient. In addition, the proposed network is able to handle complex bases, such as a Fourier basis. Benefiting from the multi-neuron layer, multiple channels of a signal can be reconstructed simultaneously.

The rest of the paper is organized as follows. The formalization of compressive sensing into a machine-learning task is explained in Section 2.1. Detailed architecture of the network and mathematics are given in Section 2.2. For method validation, a numerical example using synthetic signals is presented and discussed in Section 3.1, followed by another example using extensive field test wireless data in Section 3.2. Finally, discussion and conclusions are drawn in Section 4.

## 2 Machine-learning approach for CS data reconstruction

### 2.1 Formalizing CS into a machine-learning task

Suppose there are  $K$  sensors (channels) implemented on a structure. Each channel of the sensors is sampled  $N$  points uniformly in duration  $T$ , i.e., the sampling frequency is  $f_s = N/T$ . Collecting all the data, we obtain an  $N \times K$  matrix  $\mathbf{U}$ ,

$$\mathbf{U} = \begin{bmatrix} u_{11} & \cdots & u_{1K} \\ \vdots & u_{nk} & \vdots \\ u_{N1} & \cdots & u_{NK} \end{bmatrix}, \mathbf{U} \in \mathbb{R}^{N \times K}, \quad (3)$$

where  $u_{nk}$  is the data measured by the  $k$ th sensor at time  $t_n$ .

Then, let  $\mathbf{P}$  denote a masking matrix to random sample the original signals  $\mathbf{U}$  via element-wise multiplication, in which all elements inside are either 0 or 1 in the Bernoulli distribution with sampling ratio  $\gamma$  [Eq. (4)]. The sampled signal matrix  $\mathbf{Y}$  is then  $\mathbf{Y} = \mathbf{P} \odot \mathbf{U}$ , and the problem is how to calculate the original signal matrix  $\mathbf{U}$  from the given signal matrix  $\mathbf{Y}$ :

$$f(p_{nk}) = \begin{cases} \gamma & \text{for } p_{nk} = 1 \\ 1 - \gamma & \text{for } p_{nk} = 0 \end{cases}, p_{nk} \in \mathbf{P} \in \mathbb{Z}^{N \times K}. \quad (4)$$

As mentioned above, CS is an ill-posed inverse problem with a general representation like Eq. (5). When facing multiple signals simultaneously, which is commonly encountered, the CS problem of Eq. (2) can be represented based on “simultaneous sparsity”<sup>54, 55</sup> or “joint sparsity”<sup>56</sup> in different areas as follows:

$$\mathbf{U} = \mathbf{\Psi}\mathbf{X} + \mathbf{e}, \mathbf{\Psi} \in \mathbb{C}^{N \times N}, \mathbf{X} \in \mathbb{C}^{N \times K}, \mathbf{e} \in \mathbb{C}^{N \times K}, \quad (5)$$

where  $\mathbf{X}$  is the basis coefficient matrix of  $N$  points and  $K$  channels,  $\mathbf{\Psi}$  the basis matrix, and  $\mathbf{e}$  the error. The basis coefficient matrix  $\mathbf{X}$  is reconstructed by solving the following optimization problem:<sup>33</sup>

$$\min_{\mathbf{X} \in \mathbb{C}^{N \times K}} \|\hat{\mathbf{X}}\|_1 + \frac{\mu}{2} \|\mathbf{P} \odot \mathbf{U} - \mathbf{P} \odot \mathbf{\Psi}\hat{\mathbf{X}}\|_2, \quad (6)$$

where  $\hat{\mathbf{X}}$  is the possible solution of the Fourier coefficients matrix and  $\mu$  the penalty weight. Once the optimal solution  $\mathbf{X}_{rec}$  is obtained, the reconstructed signal matrix is given by

$$\mathbf{U}_{rec} = \mathbf{\Psi}\mathbf{X}_{rec}. \quad (7)$$

It is shown that the form of Eq. (6) is equivalent to the loss function of a regression task with regularization of parameters in the context of machine learning. Figure 1(a) illustrates the mind map of formalizing CS into a supervised-learning task. One can consider the prior knowledge, i.e., the basis matrix and the CS-sampled signals as input and output, respectively; each row of them constitutes a pair of samples as shown in Figure 1(b). The basis coefficient matrix and masking matrix are embedded into a machine neural network as weights and neurons, respectively. Then, the computation process of conventional CS is constructed as the feed-forward of the network. Different from a regular black-box neural network, the proposed network for data reconstruction is prior-knowledge-embedded and interpretable for each layer. Mathematics and examples of the network are given in the following subsections.

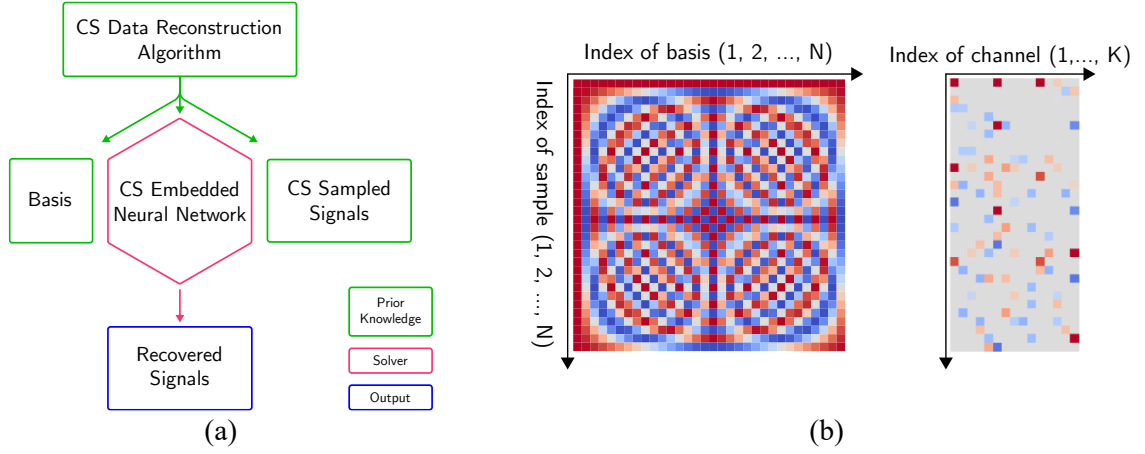


Figure 1. (a) Mind map of formalizing CS problem into a supervised-learning task; (b) example of input of network for data reconstruction

## 2.2 Construction of the novel CS-embedded neural network

As shown in Figure 2, the proposed network consists of four modules: input, basis coefficients solving, masking, and output. In the first module, the basis matrix  $\Psi$  acts as the input, and each row of the basis matrix is a training sample. For example, a basis matrix  $\Psi$  of dimension  $1024 \times 1024$  will generate 1024 samples, and the size of each sample is  $1 \times 1024$ . Note that the proposed network is able to handle complex bases, such as a Fourier basis. The real and imaginary parts of the basis are input into the network separately. If the basis matrix is real, then the imaginary-part inputs are all zero. Meanwhile, the disassembled use of the large-scale basis makes the method memory-efficient because there is no need to load the basis matrix into memory all at once.

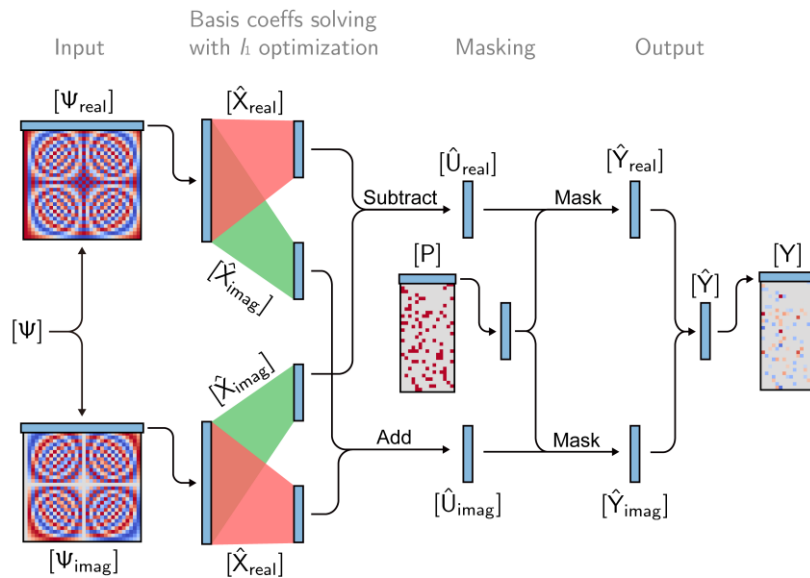


Figure 2. Architecture of the proposed network for data reconstruction

$$\mathbf{\Psi}_{real} = \begin{bmatrix} \varphi_{11}^{real} & \cdots & \varphi_{1N}^{real} \\ \vdots & \varphi_{nn}^{real} & \vdots \\ \varphi_{N1}^{real} & \cdots & \varphi_{NN}^{real} \end{bmatrix}, \mathbf{\Psi}_{real} \in \mathbb{R}^{N \times N}, \quad (8)$$

$$\mathbf{\Psi}_{imag} = \begin{bmatrix} \varphi_{11}^{imag} & \cdots & \varphi_{1N}^{imag} \\ \vdots & \varphi_{nn}^{imag} & \vdots \\ \varphi_{N1}^{imag} & \cdots & \varphi_{NN}^{imag} \end{bmatrix}, \mathbf{\Psi}_{imag} \in \mathbb{R}^{N \times N}, \quad (9)$$

$$\mathbf{\Psi} = \mathbf{\Psi}_{real} + i \cdot \mathbf{\Psi}_{imag}, \mathbf{\Psi} \in \mathbb{C}^{N \times N}. \quad (10)$$

Accordingly, the basis coefficient matrix  $\mathbf{X}$  is written as follows:

$$\mathbf{X}_{real} = \begin{bmatrix} x_{11}^{real} & \cdots & x_{1K}^{real} \\ \vdots & x_{nk}^{real} & \vdots \\ x_{N1}^{real} & \cdots & x_{NK}^{real} \end{bmatrix}, \mathbf{X}_{real} \in \mathbb{R}^{N \times K}, \quad (11)$$

$$\mathbf{X}_{imag} = \begin{bmatrix} x_{11}^{imag} & \cdots & x_{1K}^{imag} \\ \vdots & x_{nk}^{imag} & \vdots \\ x_{N1}^{imag} & \cdots & x_{NK}^{imag} \end{bmatrix}, \mathbf{X}_{imag} \in \mathbb{R}^{N \times K}, \quad (12)$$

$$\mathbf{X} = \mathbf{X}_{real} + i \cdot \mathbf{X}_{imag}, \mathbf{X} \in \mathbb{C}^{N \times K}. \quad (13)$$

In the basis-coefficients-solving module, the real and imaginary parts of the basis coefficients are embedded as two sets of weights between the input layer and first hidden layer, which are expressed in red and green, respectively, in Figure 2. For the first hidden layer, the activation function of each neuron is simply the linear function  $f(x) = x$ , which is omitted in the following equations. Note that there is a set of mirrors of  $\mathbf{X}_{real}$  and  $\mathbf{X}_{imag}$  for the complex operation. The architecture of the basis-coefficients-solving layer is determined by the complex algorithm as follows:

$$\begin{aligned} \mathbf{\Psi} &= \mathbf{\Psi}_{real} + i \cdot \mathbf{\Psi}_{imag}, \\ \hat{\mathbf{U}} &= \mathbf{\Psi} \hat{\mathbf{X}} = (\mathbf{\Psi}_{real} \hat{\mathbf{X}}_{real} - \mathbf{\Psi}_{imag} \hat{\mathbf{X}}_{imag}) + i \cdot (\mathbf{\Psi}_{real} \hat{\mathbf{X}}_{imag} + \mathbf{\Psi}_{imag} \hat{\mathbf{X}}_{real}), \hat{\mathbf{U}} \in \mathbb{C}^{N \times K}. \end{aligned} \quad (14)$$

The masking module is designed to sample the reconstructed signal matrix  $\hat{\mathbf{U}}$  by  $\mathbf{P}$  as follows:

$$\hat{\mathbf{Y}} = \mathbf{P} \odot \hat{\mathbf{U}}, \hat{\mathbf{Y}} \in \mathbb{C}^{N \times K}, \quad (15)$$

where  $\hat{\mathbf{Y}}$  denotes the masked reconstructed signals. In real-world applications, the masking matrices embedded in the transmitter and receiver are identical. Then, in the output layer, the target is the given signals  $\mathbf{Y}$ .

The loss function of the network is twofold: one is the mean-squared error (MSE) that measures the

error between the masked reconstructed signals  $\hat{\mathbf{Y}}$  and the actual sampled signals  $\mathbf{Y}$ ; another is the  $l_1$  regularizer that applies penalties on the weights  $\mathbf{X}_{real}$  and  $\mathbf{X}_{imag}$  during optimization. The loss function is given as

$$\begin{aligned} L &= \frac{1}{K} \sum_{n=1}^N \sum_{k=1}^K (y_{nk} - \hat{y}_{nk})^2 + \frac{\mu}{2} (\|\mathbf{X}_{real}\|_1 + \|\mathbf{X}_{imag}\|_1) \\ &= \frac{1}{K} \sum_{n=1}^N \sum_{k=1}^K (y_{nk} - \hat{y}_{nk})^2 + \frac{\mu}{2} \sum_{n=1}^N \sum_{k=1}^K (|x_{nk}^{real}| + |x_{nk}^{imag}|), \end{aligned} \quad (16)$$

where the lower-case variables denote the elements of corresponding matrix. So far, the feed-forward procedure has been established. In this work, we use the Adam<sup>57</sup> algorithm [Eq. (17)] to optimize the random initialized basis coefficients due to its superior convergence performance by combining stochastic gradient descent with momentum<sup>58</sup> (SGDM) and root-mean-square propagation<sup>59</sup> (RMSProp):

$$\begin{aligned} u_{\mathbf{X}}^{(t+1)} &= \beta_1 u_{\mathbf{X}}^{(t)} + (1 - \beta_1) \nabla_{\mathbf{X}} L^{(t)}, \\ v_{\mathbf{X}}^{(t+1)} &= \beta_2 v_{\mathbf{X}}^{(t)} + (1 - \beta_2) (\nabla_{\mathbf{X}} L^{(t)})^2, \\ \hat{u}_{\mathbf{X}} &= \frac{u_{\mathbf{X}}^{(t+1)}}{1 - (\beta_1)^{t+1}}, \\ \hat{v}_{\mathbf{X}} &= \frac{v_{\mathbf{X}}^{(t+1)}}{1 - (\beta_2)^{t+1}}, \\ \mathbf{X}^{(t+1)} &= \mathbf{X}^{(t)} - \eta \frac{\hat{u}_{\mathbf{X}}}{\sqrt{\hat{v}_{\mathbf{X}} + \varepsilon}}, \end{aligned} \quad (17)$$

where  $\mathbf{X}$  refers to both  $\mathbf{X}_{real}$  and  $\mathbf{X}_{imag}$  for simplicity,  $t$  denotes the step of iteration,  $u_{\mathbf{X}}^{(t)}$  is the gradient with momentum of  $\mathbf{X}$ ,  $v_{\mathbf{X}}^{(t)}$  the gradient with second momentum of  $\mathbf{X}$ ,  $\nabla_{\mathbf{X}} L^{(t)}$  the gradient of  $L^{(t)}$  with respect to  $\mathbf{X}$ , and  $\beta_1$   $\beta_2$  are the respective hyperparameters used to weight the momentum and second momentum terms.

Once we obtain the reconstructed signals, the reconstruction error between the original and reconstructed signals is calculated by

$$\xi = \left| \frac{\|\mathbf{U} - \mathbf{U}_{rec}\|_2}{\|\mathbf{U}\|_2} \right|_{col}, \quad (18)$$

where  $|\cdot|_{col}$  denotes column-wise operation, i.e., the norm is separately calculated for each channel;

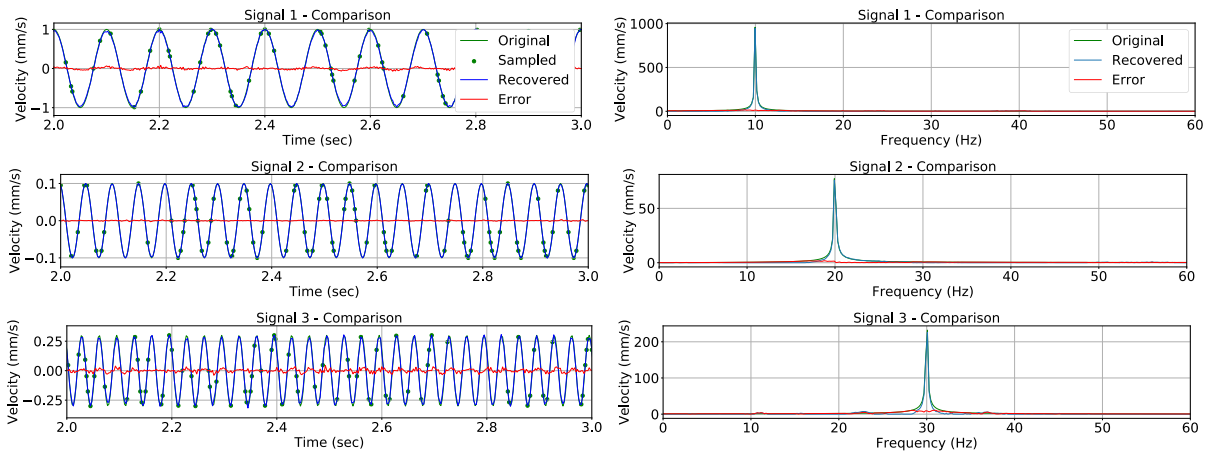
therefore, the reconstruction error  $\xi$  is a row vector of dimension  $1 \times K$ .

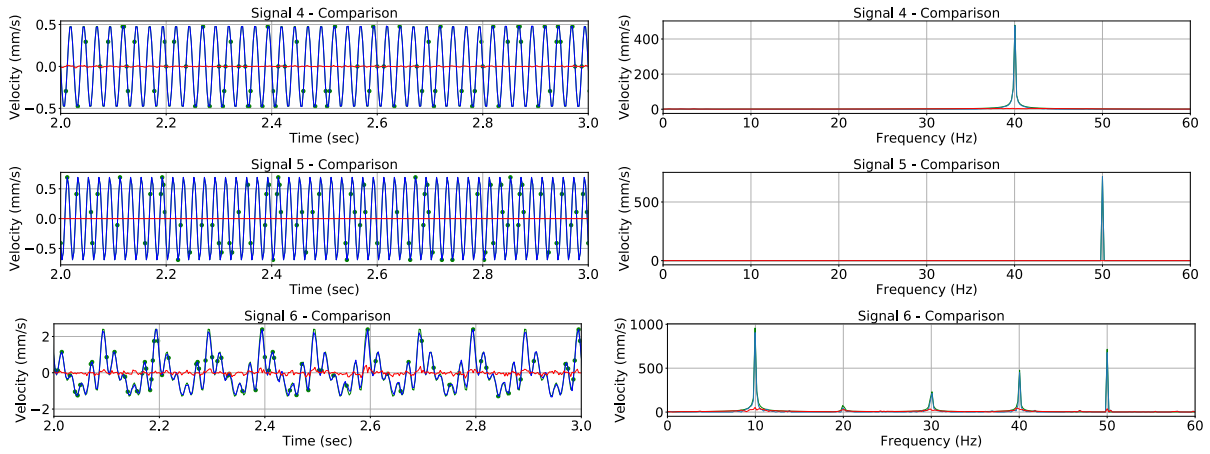
### 3 Examples

#### 3.1 Examples using simple synthetic signals

To validate the performance of the proposed CS-embedded network for data reconstruction, numerical simulations were conducted on multiple sinusoidal waves. First, five sinusoidal waves of frequency 10, 20, 30, 40, and 50 Hz were generated at a sampling frequency  $f_s = 400$  Hz ; then, a superposed wave was synthesized from the first five waves by linear superposition. All six waves were sampled at  $\gamma = 0.2$  by the masking module of the network; therefore, the equivalent sampling frequency is 80 Hz, which is already lower than twice the maximum predominant frequency (50 Hz) of signals 5 and 6, thus breaking the Nyquist-Shannon sampling theorem. The specific expressions of each simulated signal are given in Eq. (19). A Fourier-basis matrix of dimension  $2048 \times 2048$  is used as the input; correspondingly, the original signal matrix is split into four matrices of dimension  $2048 \times 6$  (i.e., 5.12 s in duration) as the targets:

$$\begin{aligned}
 T &= 20.48 \text{ s} , f_s = 400 \text{ Hz} , \\
 t &\in [0, T] , dt = 1 / f_s = 0.0025 \text{ s} , \\
 s_n &= A_n \cos(2\pi \cdot f_n \cdot t + \text{phase}_n) , \\
 \left\{ \begin{aligned}
 s_1 &= \cos(2\pi \cdot 10 \cdot t) , \\
 s_2 &= 0.1 \cdot \cos(2\pi \cdot 20 \cdot t + 0.1\pi) , \\
 s_3 &= 0.3 \cdot \cos(2\pi \cdot 30 \cdot t + 0.3\pi) , \\
 s_4 &= 0.5 \cdot \cos(2\pi \cdot 40 \cdot t + 0.5\pi) , \\
 s_5 &= 0.7 \cdot \cos(2\pi \cdot 50 \cdot t + 0.7\pi) , \\
 s_6 &= s_1 + s_2 + s_3 + s_4 + s_5 .
 \end{aligned} \right. \quad (19)
 \end{aligned}$$

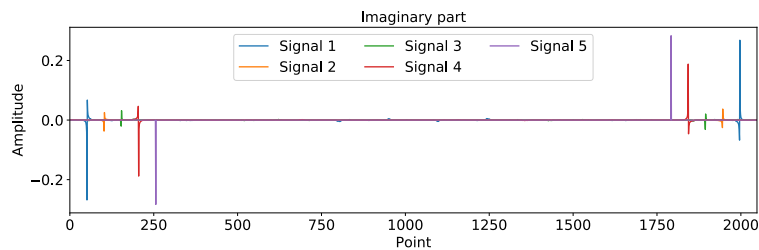
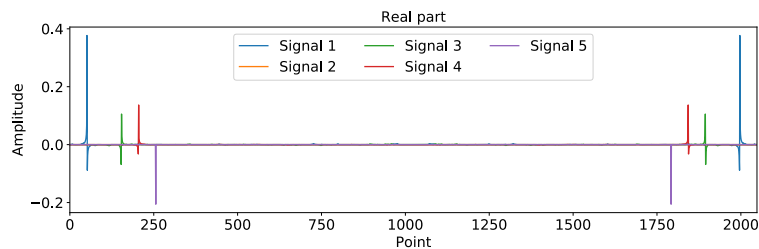




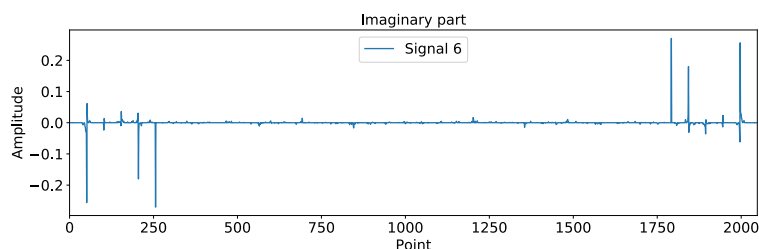
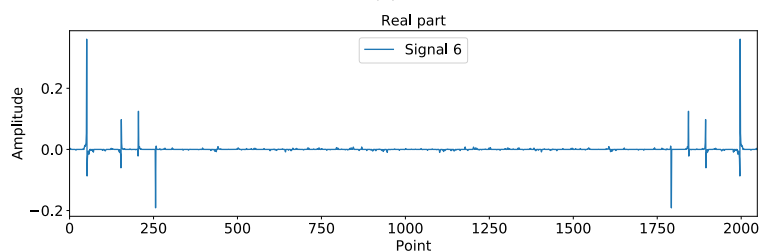
(a)

(b)

Figure 3. Comparison between original signals and reconstructed signals (time responses are displayed for 1 s for visibility): (a) time domain; (b) frequency domain



(a)



(b)

Figure 4. Reconstructed basis coefficients of each signal: (a) signals 1–5; (b) signal 6

The comparison results in Figure 3 show that although the sampled points are quite sparse, all six

signals are well reconstructed both in the time and frequency domains. Signals 5 and 6 even achieved better reconstruction compared with the other signal channels. Moreover, without any constraints except for  $l_1$ -norm minimization for  $\mathbf{X}$ , in Figure 4 the real and imaginary parts of the reconstructed basis coefficients show the fine characteristics of even and odd symmetry, respectively, which agree on the nature of the Fourier basis.

### 3.2 Examples using field test wireless data of a long-span bridge

Next, we used more complex data collected from a field test on Xiamen Haicang Bridge to evaluate the performance of the proposed approach. As shown in Figure 5(a), the bridge is a steel-box-girder suspension bridge with a span distribution of 230 m+648 m+230 m, two towers with a height of 140 m, and a bridge deck 32 m wide. To avoid disturbing the normal traffic, the test was carried out at midnight. The test schemes are shown in Figure 6. Specifically, the tests were repeated nine times and tested a total of 62 test points. Test 1 had seven test points (Nos. 1–6 and No. 26); wireless sensors were placed on the seven test points to measure the vibration data. The time duration of each test was 20 min. After Test 1 finished, the wireless sensors were moved for Test 2, which also included seven test points (Nos. 7–12 and No. 26). Considering the effective wireless-data-transmission distances, test point No. 26 was selected as the reference point for all nine tests. Tests 3–9 were conducted in the same way. The field test used nine commercial wireless velocity sensors as shown in Figure 5(b); the sampling frequency for data acquisition was 100 Hz.

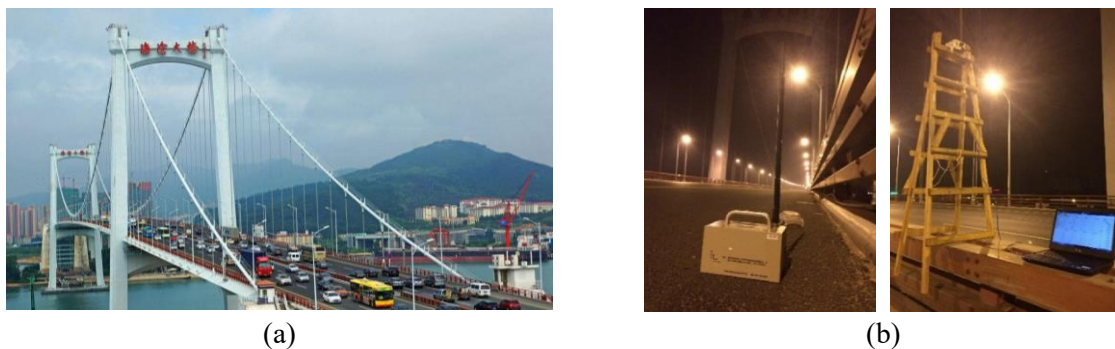


Figure 5. (a) Xiamen Haicang Bridge; (b) wireless sensor and base station

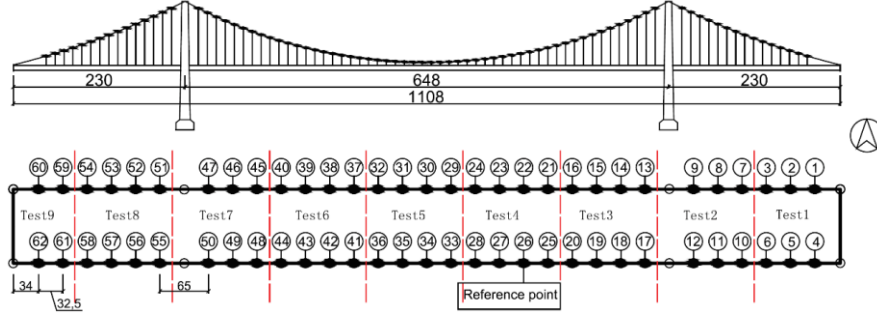
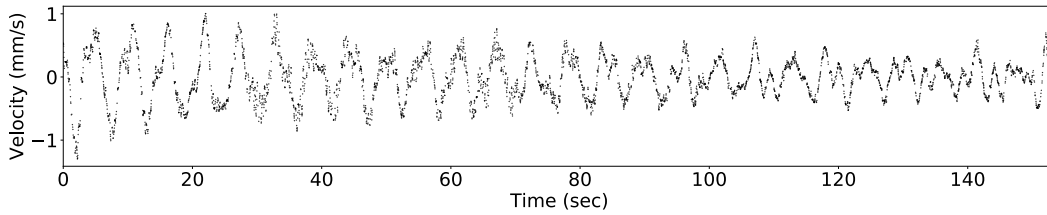


Figure 6. Placement of test points

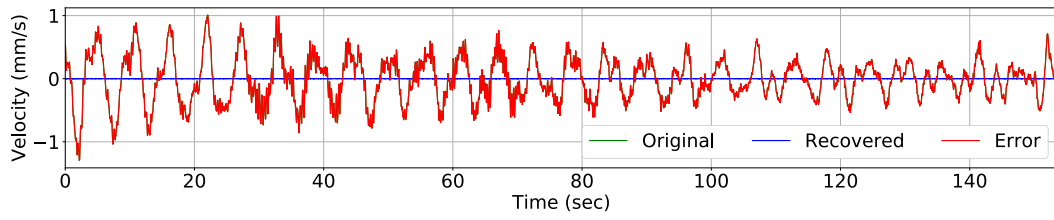
We simulate the CS-sampling procedure at nine different sampling ratios ranging from 10% to 50% in steps of 5% for all 62 points. The length of the signal slice and the dimension of the basis matrix are both set to 2048. Table 1 lists the schedule of parameters during optimization. It is found that the real part of the signal is slower to converge in the optimization procedures, so the loss weight pair is introduced in the output layer to magnify the loss individually, which mainly speeds up the training of the real part. Figure 7 and Figure 8 demonstrate the typical signal-reconstruction process (Test 2, point 26,  $\gamma=0.3$ ). Specifically, Figure 7 visualizes the reconstructed time response at epochs 100, 150, 200, 400, and 600. It is shown that the reconstructed response remains almost zero after 100 epochs of training; then, it gradually converges to the original. Figure 8 shows the loss history of  $\mathbf{X}_{real}$  and  $\mathbf{X}_{imag}$ , as well as the evolution of the shapes of  $\mathbf{X}_{real}$  and  $\mathbf{X}_{imag}$ .

Table 1 Schedule of parameters during optimization

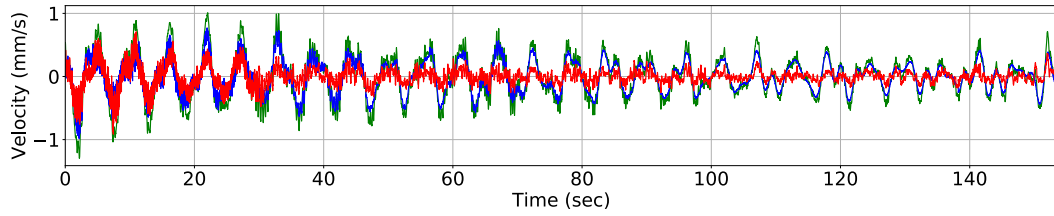
Epoch	Learning rate	Loss weight		Batch size
		Real part	Imaginary part	
1–100		1	1	
101–200	0.0001	128	1	
201–300		256	1	128
301–400		1024	1	
401–500	0.00001	4096	512	
501–600		8192	512	



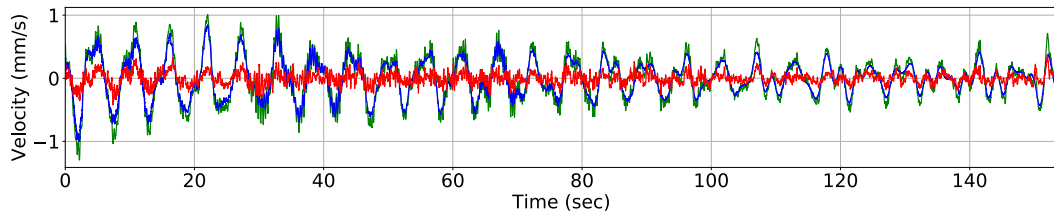
(a)



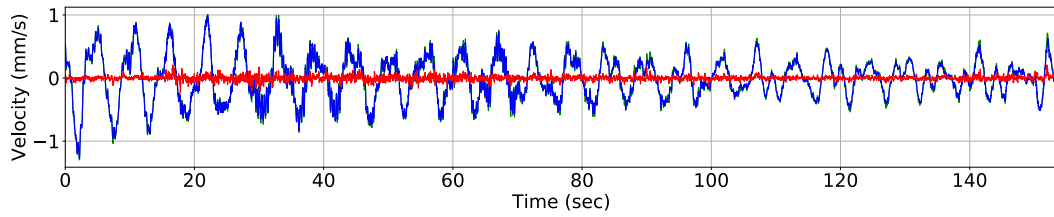
(b)



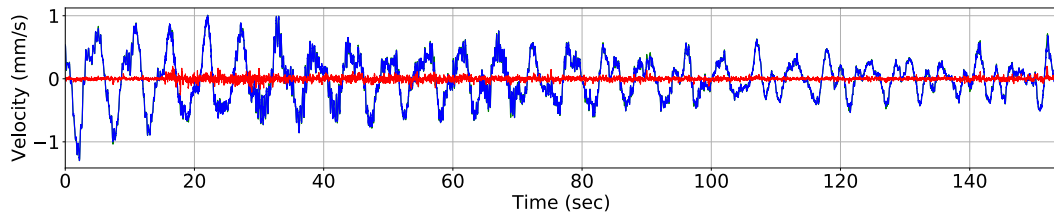
(c)



(d)

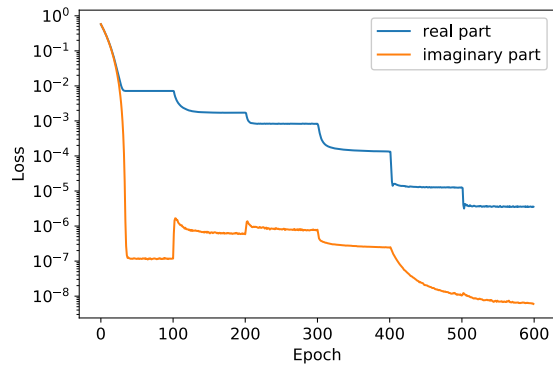


(e)

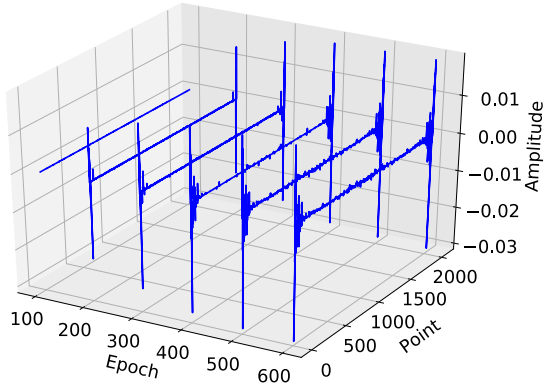


(f)

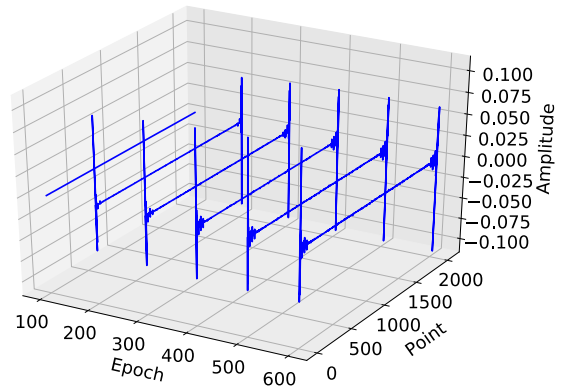
Figure 7. (a) Sampled data with sampling ratio 0.3 of Test 2, point 26; (b)–(f) typical signal-reconstruction process at epochs 100, 150, 200, 400, and 600, respectively.



(a)



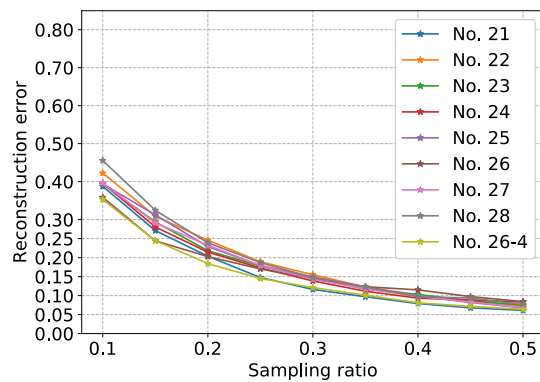
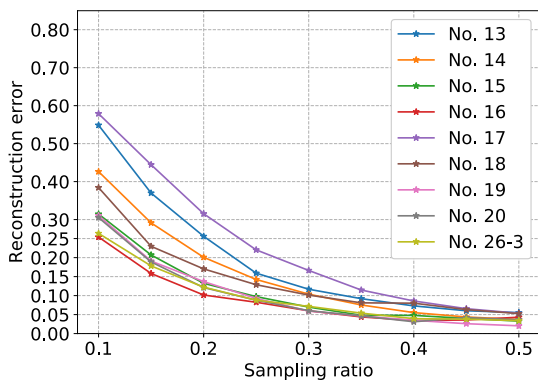
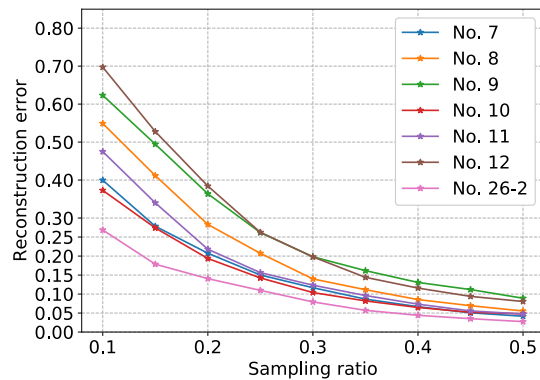
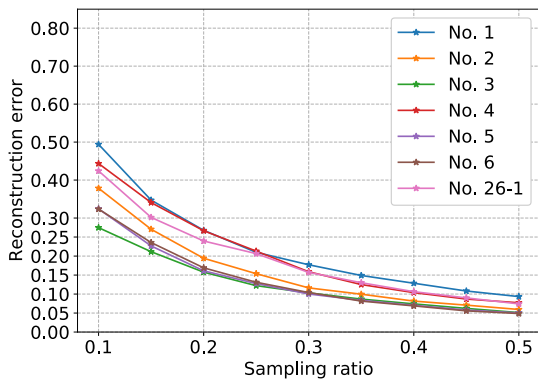
(b)



(c)

Figure 8. Optimization process of basis coefficients at sampling ratio 0.3 of Test 2, point 26: (a) loss history; (b) real part; (c) imaginary part

Nine grouped test results in Figure 9 show the consistent decrease of reconstruction error as the sampling ratio increases from 10% to 50% in steps of 5%. At a sampling ratio of 0.3, the best reconstruction appears at Test 6, channel 7, which achieves an error of only 0.0474; meanwhile, the reconstruction errors of other signals are approximately 0.1; at a sampling ratio of 0.5, again, channel 7 of Test 6 accomplishes the minimal reconstruction error of 0.0196; other signals are reconstructed with errors ranging approximately between 0.05 and 0.1.



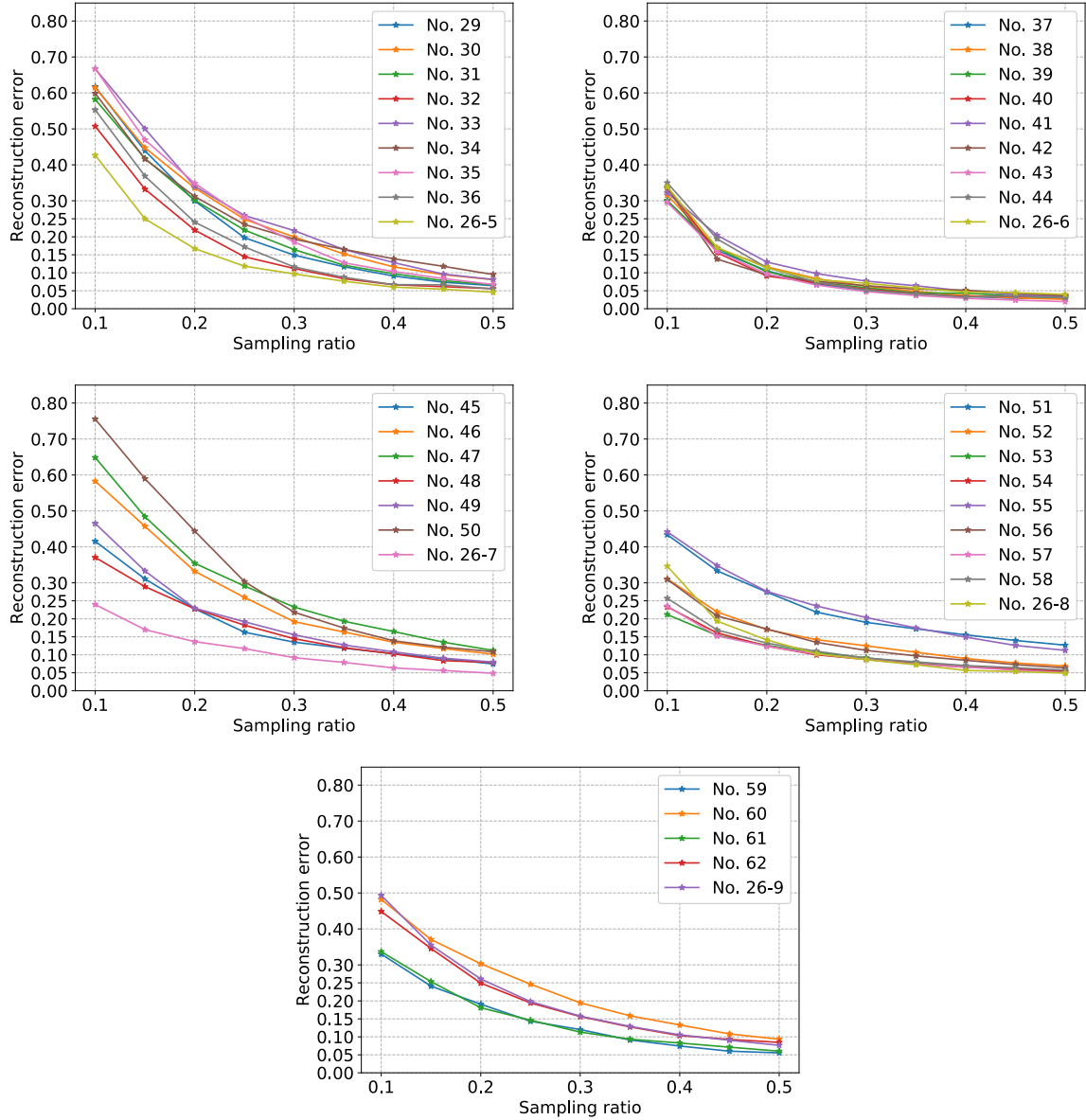


Figure 9. Simulation results based on field-test wireless data (nine tests are given by row)

## 4 Discussion and conclusions

In this paper, we proposed a novel neural network approach to solve the CS data-reconstruction problem. The prior knowledge, i.e., the Fourier-basis matrix and CS-sampled signals, are used as the input and the target of the network; the coefficient matrix is embedded as the parameters of a certain layer; and the objective function of conventional CS is set as the loss function of the network. Regularized by  $l_1$ -norm, these basis coefficients are optimized to reduce the error between the original CS-sampled signals and masked reconstructed signals with a common gradient-descent optimization algorithm. Multiple signal channels can be reconstructed simultaneously. Validations using numerical data and field-test data

show that data can be well reconstructed with low sampling ratio.

It is noteworthy that, although the neural network-based approach was used only to reconstruct the time-series SHM data, it is an open architecture for other conventional optimization problems. Essentially, a neural network can be considered as a computation graph, in which other objective functions or regularizations can be mapped into as elements such as nodes or weights. The integration of classical optimization problems and machine-learning techniques not only enables neural networks to be used to solve conventional optimization, but also makes the neural network interpretable and more trustworthy for users, which promotes the incorporation of machine-learning techniques into processes with well-grounded rationales or critical outputs. In the big data and AI times, machine learning will have a good potential to solve the optimization problems in civil engineering.

## **Acknowledgment**

This research was supported by grants from the National Key R&D Program of China (Grant No. 2017YFC1500603), the National Natural Science Foundation of China (Grant No. U1711265, 51678203 and 51638007).

## **References**

1. Li H, Ou J, Zhang X, et al. Research and practice of health monitoring for long-span bridges in the mainland of China. 2015; 15: 555-576.
2. Worden K, Farrar CR, Haywood J, et al. A review of nonlinear dynamics applications to structural health monitoring. *Struct Control Hlth* 2008; 15: 540-567.
3. Farrar CR and Worden K. *Structural health monitoring: a machine learning perspective*. John Wiley & Sons, 2012.
4. Ihn J-B and Chang F-K. Pitch-catch active sensing methods in structural health monitoring for aircraft structures. *Struct Health Monit* 2008; 7: 5-19.
5. Spencer BF, Ruiz - Sandoval ME and Kurata N. Smart sensing technology: opportunities and challenges. *Struct Control Hlth* 2004; 11: 349-368.

6. Chang PC, Flatau A and Liu S. Health monitoring of civil infrastructure. *Struct Health Monit* 2003; 2: 257-267.
7. Ou J and Li H. Structural health monitoring in mainland China: review and future trends. *Struct Health Monit* 2010; 9: 219-231.
8. Ko J and Ni Y. Technology developments in structural health monitoring of large-scale bridges. *Eng Struct* 2005; 27: 1715-1725.
9. Donoho DL. Compressed sensing. *IEEE T Inform Theory* 2006; 52: 1289-1306.
10. Candès EJ. Compressive sampling. In: *Proceedings of the international congress of mathematicians* 2006, pp.1433-1452. Madrid, Spain.
11. Chen SS, Donoho DL and Saunders MA. Atomic decomposition by basis pursuit. *SIAM Rev* 2001; 43: 129-159.
12. Figueiredo MA, Nowak RD and Wright SJ. Gradient projection for sparse reconstruction: Application to compressed sensing and other inverse problems. *IEEE J-STSP* 2007; 1: 586-597.
13. Lustig M, Donoho D and Pauly JM. Sparse MRI: The application of compressed sensing for rapid MR imaging. *Magnetic Resonance in Medicine: An Official Journal of the International Society for Magnetic Resonance in Medicine* 2007; 58: 1182-1195.
14. Hale ET, Yin W and Zhang Y. Fixed-point continuation for  $l_1$ -minimization: Methodology and convergence. *SIAM J Optimiz* 2008; 19: 1107-1130.
15. Wen Z, Yin W, Goldfarb D, et al. A fast algorithm for sparse reconstruction based on shrinkage, subspace optimization, and continuation. *SIAM J Sci Comput* 2010; 32: 1832-1857.
16. Goldstein T and Osher S. The split Bregman method for  $L_1$ -regularized problems. *SIAM J Imaging Sci* 2009; 2: 323-343.
17. Beck A and Teboulle M. A fast iterative shrinkage-thresholding algorithm for linear inverse problems. *SIAM J Imaging Sci* 2009; 2: 183-202.
18. Wright SJ, Nowak RD and Figueiredo MA. Sparse reconstruction by separable approximation. *IEEE T Signal Process* 2009; 57: 2479-2493.
19. Becker S, Bobin J and Candès EJ. NESTA: A fast and accurate first-order method for sparse recovery. *SIAM J Imaging Sci* 2011; 4: 1-39.

20. Ji S, Xue Y and Carin L. Bayesian compressive sensing. *IEEE T Signal Process* 2008; 56: 2346.
21. Yuan M and Lin Y. Model selection and estimation in regression with grouped variables. *Journal of the Royal Statistical Society: Series B (Statistical Methodology)* 2006; 68: 49-67. DOI: 10.1111/j.1467-9868.2005.00532.x.
22. Takhar D, Laska JN, Wakin MB, et al. A new compressive imaging camera architecture using optical-domain compression. In: *Computational Imaging IV* 2006, p.606509. International Society for Optics and Photonics.
23. Duarte MF, Davenport MA, Takhar D, et al. Single-pixel imaging via compressive sampling. *IEEE Signal Proc Mag* 2008; 25: 83-91.
24. Ma J. Single-pixel remote sensing. *J IEEE Geoscience Remote Sensing Letters* 2009; 6: 199-203.
25. Herrmann FJ, Friedlander MP and Yilmaz O. Fighting the curse of dimensionality: Compressive sensing in exploration seismology. *IEEE Signal Proc Mag* 2012; 29: 88-100.
26. Luo C, Wu F, Sun J, et al. Compressive data gathering for large-scale wireless sensor networks. In: *Proceedings of the 15th annual international conference on Mobile computing and networking* 2009, pp.145-156. ACM.
27. Caione C, Brunelli D and Benini L. Compressive sensing optimization for signal ensembles in WSNs. *IEEE T Ind Inform* 2014; 10: 382-392.
28. Klis R and Chatzi EN. Vibration monitoring via spectro-temporal compressive sensing for wireless sensor networks. *Struct Infrastruct E* 2017; 13: 195-209.
29. O'Connor S, Lynch J and Gilbert A. Compressed sensing embedded in an operational wireless sensor network to achieve energy efficiency in long-term monitoring applications. *Smart Mater Struct* 2014; 23: 085014.
30. Bao Y, Li H, Sun X, et al. Compressive sampling-based data loss recovery for wireless sensor networks used in civil structural health monitoring. *Struct Health Monit* 2013; 12: 78-95.
31. Zou Z, Bao Y, Li H, et al. Embedding compressive sensing-based data loss recovery algorithm into wireless smart sensors for structural health monitoring. *IEEE Sens J* 2015; 15: 797-808.
32. Yang Y and Nagarajaiah S. Harnessing data structure for recovery of randomly missing structural vibration responses time history: Sparse representation versus low-rank structure. *Mech Syst Signal*

- Pr* 2016; 74: 165-182.
33. Bao Y, Shi Z, Wang X, et al. Compressive sensing of wireless sensors based on group sparse optimization for structural health monitoring. *Struct Health Monit* 2017; 1475921717721457.
  34. Peckens C and Lynch J. Utilizing the cochlea as a bio-inspired compressive sensing technique. *Smart Mater Struct* 2013; 22: 105027.
  35. Park JY, Wakin MB and Gilbert AC. Modal Analysis With Compressive Measurements. *IEEE T Signal Process* 2014; 62: 1655-1670.
  36. Yang Y and Nagarajaiah S. Output-only modal identification by compressed sensing: Non-uniform low-rate random sampling. *Mech Syst Signal Pr* 2015; 56: 15-34.
  37. Wang Y and Hao H. Damage identification scheme based on compressive sensing. *J Comput Civil Eng* 2013; 29: 04014037.
  38. Yao R, Pakzad SN and Venkitasubramaniam P. Compressive sensing based structural damage detection and localization using theoretical and metaheuristic statistics. *Struct Control Hlth* 2017; 24: e1881.
  39. Zhou S, Bao Y and Li H. Structural damage identification based on substructure sensitivity and  $l_1$  sparse regularization. In: *Sensors and Smart Structures Technologies for Civil, Mechanical, and Aerospace Systems 2013* 2013, p.86923N. International Society for Optics and Photonics.
  40. Zhou X-Q, Xia Y and Weng S.  $l_1$  regularization approach to structural damage detection using frequency data. *Struct Health Monit* 2015; 14: 571-582.
  41. Zhang C and Xu Y. Comparative studies on damage identification with Tikhonov regularization and sparse regularization. *Struct Control Hlth* 2016; 23: 560-579.
  42. Hou R, Xia Y, Bao Y, et al. Selection of regularization parameter for  $l_1$ -regularized damage detection. *J Sound Vib* 2018; 423: 141-160.
  43. Bao Y, Li H, Chen Z, et al. Sparse  $l_1$  optimization - based identification approach for the distribution of moving heavy vehicle loads on cable - stayed bridges. *Struct Control Hlth* 2016; 23: 144-155.
  44. Sun J, Li H and Xu Z. Deep ADMM-Net for compressive sensing MRI. In: *Advances in Neural Information Processing Systems* 2016, pp.10-18.

45. Jin KH, McCann MT, Froustey E, et al. Deep convolutional neural network for inverse problems in imaging. 2017; 26: 4509-4522.
46. Adler J and Öktem O. Solving ill-posed inverse problems using iterative deep neural networks. *Inverse Probl* 2017; 33: 124007. DOI: 10.1088/1361-6420/aa9581.
47. Bruna J, Sprechmann P and LeCun Y. Super-resolution with deep convolutional sufficient statistics. *arXiv preprint arXiv:05666* 2015.
48. Putzky P and Welling MJ. Recurrent inference machines for solving inverse problems. 2017.
49. Chang J-HR, Li C-L, Póczos B, et al. One Network to Solve Them All-Solving Linear Inverse Problems using Deep Projection Models. In: *ICCV 2017*, pp.5889-5898.
50. Zhang R, Isola P and Efros AA. Colorful image colorization. In: *European Conference on Computer Vision 2016*, pp.649-666. Springer.
51. Larsson G, Maire M and Shakhnarovich G. Learning representations for automatic colorization. In: *European Conference on Computer Vision 2016*, pp.577-593. Springer.
52. Hershey JR, Roux JL and Wenginger F. Deep unfolding: Model-based inspiration of novel deep architectures. *arXiv preprint arXiv:14092574* 2014.
53. Kavi KM, Buckles BP and Bhat UN. A formal definition of data flow graph models. *IEEE T Comput* 1986: 940-948.
54. Tropp JA, Gilbert AC and Strauss MJ. Algorithms for simultaneous sparse approximation. Part I: Greedy pursuit. *Signal Process* 2006; 86: 572-588.
55. Tropp JA. Algorithms for simultaneous sparse approximation. Part II: Convex relaxation. *Signal Process* 2006; 86: 589-602.
56. Fornasier M and Rauhut H. Recovery algorithms for vector-valued data with joint sparsity constraints. *SIAM J Numer Anal* 2008; 46: 577-613.
57. Kingma DP and Ba J. Adam: A method for stochastic optimization. *arXiv preprint arXiv:14126980* 2014.
58. Rumelhart DE, Hinton GE and Williams RJ. Learning representations by back-propagating errors. *nature* 1986; 323: 533.
59. Tieleman T and Hinton G. Lecture 6.5-rmsprop: Divide the gradient by a running average of its

recent magnitude. *COURSERA: Neural networks for machine learning* 2012; 4: 26-31.